# Acoustic Shadow Detection From Scanline Statistics of B-Mode and Radiofrequency Ultrasound Images of Different Anatomy and Transducers

Ricky Hu[a,*], Rohit Singla[a], Farah Deeba[a], Robert N. Rohling[a]

[a]*Department of Electrical and Computer Engineering, University of British Columbia, Vancouver, Canada*

## Abstract

An acoustic shadow is an ultrasound artifact occurring at boundaries between significantly different materials, resulting in a continuous dark region on the image. Shadow detection is important as shadows can identify anatomical features or obscure regions of interest. A study was performed to scan human subjects (N=35) specifically to explore the statistical characteristics of shadows. Subjects were scanned using different transducers and anatomy for a general investigation of shadows as previous studies focused on shadows created by specific imaging scenarios. Shadow detection methods were then developed by analyzing the statistics of patches of radiofrequency (RF) or brightness-mode (B-mode) data if RF data is unavailable. Both methods utilized adaptive thresholding, needing only the pulse width of the transducer as an input parameter for easy utilization by different operators or equipment. Mean Dice coefficients ($\pm$ standard deviation) of $0.90\pm0.07$ and $0.87\pm0.08$ were obtained for the RF and B-mode methods, which is within the Dice coefficient range between manual annotators. [COMMENT ON GENERAL SHADOW OBSERVATIONS] The results indicate that the methods are able to detect shadows with high versatility in different imaging scenarios. The method has potential to aid interpretation of ultrasound images or serve as an important pre-processing step for machine learning methods.

*Keywords:* Acoustic Shadow, Ultrasound, Speckle, Radiofrequency, Segmentation

## 1. Introduction

Ultrasound devices have become increasingly affordable and portable, encouraging applications such as point-of-care ultrasound (Bouhemad et al., 2011), novice usage (Becker et al., 2016), and creating training data sets for machine learning (Ghose et al., 2013). However, ultrasound is susceptible to unique artifacts that increase the difficult of interpretation and processing of images. One artifact is an acoustic shadow, which occurs when an ultrasound wave propagates to a boundary of two materials with high impedance differences (Kremkau and Taylor, 1986). The wave is almost completely reflected and beyond the boundary is a continuous dark region and a loss of anatomical features. Shadows occur in air-tissue, tissue-bone, and tissue-lesion interfaces. Shadows can aid interpretation, such as identifying gall stones (Good et al., 1979) or spinal levels (Galiano et al., 2005). However, shadows, such as from poor transducer contact, can lead to misinterpretation of anatomy, particularly by novice users and automated processing algorithms. Thus, the identification of shadows is an important preprocessing step in many applications.

Several methods have been used in literature to detect shadows. Geometric techniques model the path of an ultrasound signal for an expected image along the scanline using a random walk (Karamalis et al., 2012). Pixels are then flagged as a shadow if it is below a confidence threshold. However, geometric techniques require knowledge of ultrasound transducer properties to parameterize random walk weights, such as the focal length, radius of curvature, and thickness. The technique would be cumbersome to implement across different ultrasound machines. This also reduces applicability for machine learning applications as accurate transducer parameter labels are required for each image.

Pixel intensity methods ignore the transducer properties an analyze only the graphical properties of animage (Hellier et al., 2010). Shadows have been detected on brain images by analyzing the entropy along a scanline to flag pixels of sudden low entropy as a potential shadow. The technique achieved a comparable Dice similarity coefficient as geometric methods but require specific thresholding, window sizing, filtering, and image mask parameterization for different anatomy and transducers. This method would be infeasible in a clinical setting, particularly for novice users or point-of-care applications, as parameterization requires image processing expertise.

Machine learning methods have gained significant interest in medical imaging analysis. To our knowledge, no machine learning method has demonstrated capability of general shadow detection from multiple anatomy. Deep learning methods have identified features in a specific im-

---

*Corresponding Author: Ricky Hu, Robotics and Control Laboratory, University of British Columbia, Room 3090, 2332 Main Mall, Vancouver, BC, Canada V6T 1Z4. Email: rhu@ece.ubc.ca

age sets that contains a shadow, such as neuroanatomical regions in cranial scan (Milletari et al., 2017) or spinal levels in a posterior scan (Hetherington et al., 2017). Although machine learning has the potential of providing automated feature recognition in multiple applications, a large data set is required for an algorithm to recognize certain features. Ultrasound imaging is highly variable due to unique artifacts, operator technique, and equipment. In addition, shadows are a very general feature that occur in various imaging scenarios. Previous techniques focus on a single anatomical region and training data was from a consistent imaging scenario. However, it is difficult to construct a training data set with the generality required to recognize shadows in different scenarios usable for a variety of ultrasound applications.

There are two objectives to the study. First, to address the need of understanding general characteristics of shadows, a study was conducted to scan multiple anatomy and transducers specifically to analyze the statistics of different types of shadows. Second, to address existing needs for versatile detection and limiting parameterization, previous methods were then extended utilizing statistical thresholding of radiofrequency (RF) or brightness-mode (B-mode) data to detect the full range of shadows.

## Materials and Methods

### Data Collection

Ultrasound RF and B-mode data was acquired by scanning 37 adult participants with informed written consent, approved by the University of British Columbia Research Ethics Board (Study ID: H18-01199). The scans included a forearm scan near the distal end of the pronator quadratus, an elbow scan near the cubital fossa, and a rib scan on the anterior surface of right ribs 11-12. Each scan was taken with both a curvilinear (C5-2/60, Ultrasonix, Canada) and linear (L14-5/38, Ultrasonix, Canada) transducer. Different transducer settings were used for each anatomical region and transducer, summarized in Table 1. Shadows are expected to occur due to bones in the arm and from an air gap created by the lateral edges of the curvilinear transducer not being in flush contact with the skin. The experiment was designed to generate a dataset from various imaging scenarios to explore general shadow characteristics and to validate the versatility of the shadow detection methods.

### Radiofrequency Speckle Analysis

To analyze shadows, patches of speckle was analyzed on the RF signal. Speckle occurs due to multiplicative scattering of acoustic waves in a material, resulting in a granular patch on the image. The benefit of RF analysis is that B-mode image processing commonly attempts to remove speckle, but speckle contains information of the acoustic interactions in tissue (Burckhardt, 1978). Speckle can then characterize different regions, such as a region of tissue or a region of signal loss in a shadow. In addition, B-mode data can be manipulated by an operator to visually enhance an image, such as adjusting time-gain compensation or dynamic range. Thus, speckle analysis can provide shadow detection usable across different machines and operators.

One of the first models for speckle is with a one-parameter Rayleigh distribution to model the probability density of a random walk (Burckhardt, 1978). The Rayleigh distribution is capable for modeling fully developed speckle, which does not occur in limited scattering (Tuthill et al., 1988). More generalized models have been applied such as the Rician, Homodyned-K, and Nakagami distributions to characterize speckle (Destrempes and Cloutier, 2010). The utility of speckle has been demonstrated in literature to classify tumorigenicity of breast lesions (Byra et al., 2016) or levels of liver fibrosis (Ho et al., 2012) by categorizing image regions based on the speckle pattern. Shadow characterization presents a simpler problem as a shadow and non-shadow region contain significantly different speckle patterns. Thus, the Nakagami distribution expressed in Eq. 1 was chosen to model speckle. The Nakagami distribution provides greater generality than the Rayleigh distribution while being more computationally efficient than the Rician or Homodyned K distributions (Destrempes and Cloutier, 2010).

$$\Phi(x,\mu,\omega) = 2(\frac{\mu}{\omega})^\mu \frac{1}{\Gamma(\mu)} x^{(2\mu-1)} e^{\frac{-\mu}{\omega}x^2} \tag{1}$$

Where $x$ is the RF intensity, $\mu$ is the shape parameter, $\omega$ is the scale parameter and $\Gamma(\mu)$ is the gamma distribution.

To characterize shadows, the raw RF data was first processed by computing the echo envelope of each scanline with a Hilbert transform. An absolute logarithmic scale of the echo envelope was taken to generate an "RF Image", visually similar to B-mode but without filtering to remove speckle. Next, the RF image was divided into overlapped patches with a width of a single RF data point and a length of three times the pulse width. This patch size was demonstrated in literature to be sufficiently large to capture multiple wavelengths and scattering events while being small enough to be useful in differentiating different regions on the millimeter scale (Byra et al., 2016). Next, the RF data in each patch was fit to a Nakagami distribution using a maximum likelihood estimate to compute the fitted Nakagami shape and scale parameters $\mu$ and $\omega$, producing a map of Nakagami parameter values for an image as shown in Fig. 1.

To detect shadows, a simple automated thresholding scheme was used. Otsu's method was applied on the entire image to compute a threshold for the Nakagami $\omega$ parameter. This was sufficient as the Nakagami $\omega$ parameter is significantly different for shadow regions with abundant speckle and non-shadow regions with minimal speckle, Then, for each scanline, the deepest data point

that is above the threshold is labeled as the shadow boundary and all data points below are labeled as a shadow.

### B-mode Scanline Analysis

Many ultrasound machines do not provide access to RF data for speckle analysis. Thus, a previous pixel-intensity shadow detection method on B-mode images was modified and extended. Scanline entropy was investigated on B-mode images to characterize different types of shadows. Adaptive thresholding of entropy was then applied for shadow detection to address the need for usability across different equipment with minimum configuration. First, the cumulative scanline entropy is computed for each pixel, similar to the "Rupture Criterion" (Hellier et al., 2010), with the window size fixed as three times the pulse width, $\eta$, as defined in Eq. 2

$$S_{i,j} = \sum_{i=1}^{3\eta} I(i-1)log_2\frac{I(i-1)}{I(i+1)} + I(i+1)log_2\frac{I(i+1)}{I(i-1)} \quad (2)$$

Where $S_{i,j}$ is the cumulative entropy at pixel $i$ on scanline $j$, $\eta$ is the pulse width, $I(i)$ is the pixel intensity of $i$.

For linear images, tracking scanlines is simple. For curvilinear images, the scanline paths were tracked by capturing the slope of the lateral edges by following the ring-down regions. Ring-down is a consistent artifact that produces bright bands at the top of an image due to the fluid in the transducer reflecting a continuous signal. The scanlines were then interpolated between the slopes of the lateral edges.

Next, Otsu's method is applied similarly to compute a threshold entropy value. The intuition of the threshold is different than in RF analysis. In RF analysis, the threshold separates patches of intense and minimal speckle. In B-mode analysis, the threshold separates pixels of a shadow boundary, which has high entropy, and pixels not of a shadow boundary, which include shadow and non-shadow regions. Thus, shadows can be identified by finding the last pixel on a scanline with an entropy higher than the threshold, representing a bright shadow boundary.

### Validation

A trained annotator manually outlined shadow regions on B-mode images. The manual regions were used as a gold standard, as manual identification is common in clinical practice and has been used in previous literature for comparison (Hellier et al., 2010). A Dice coefficient was computed to compare similarity of manual and automated shadow detection.

### Results

Examples of detected shadows from both methods are highlighted in gray in Fig. 2 in different imaging scenarios. The Dice coefficients for both methods for different anatomy and transducers are shown in Table 2. The mean Dice coefficients (± standard deviation) were 0.90±0.07 and 0.87±0.08 for RF and B-mode methods. Manual annotation was repeated five times with a mean Dice coefficient of 0.92±0.02 for all images and transducers.

With the benefit of a varied dataset, general characteristics of shadows can be analyzed. The log-scale Nakagami $\omega$ parameter recorded a mean ± standard deviation of $13.95 \pm 2.03$ for all non-shadow and $8.89 \pm 1.16$ for shadow regions defined by manual outlining of all images. The $\mu$ parameter recorded $1.02 \pm 0.29$ for non-shadow and $3.25 \pm 2.35$ for shadow-regions. The B-mode scanline entropy was recorded to be X at shadow regions, and X at non-shadow regions.

### Discussion

The RF and B-mode shadow detection developed achieved a high Dice similarity coefficient for all anatomy and transducer types. Previous studies reported that the Dice coefficient between manual annotators recorded a mean of 0.91±0.07 (Hellier et al., 2010). Every scenario detected from both methods achieved a Dice coefficient within the range of manual detection within operator variability. This supports the versatility of the detection method as both methods are able to identify shadows across different anatomy and transducers with minimum configuration.

Separate to shadow detection, the computed Nakagami $\omega$ parameter of all manually outlined shadows indicate that there is a statistically significant difference between shadow and non-shadow regions. The speckle from shadows is distinct from the speckle created by tissue, muscle, or fat. This is likely due to physical properties of speckle, as speckle occurs due to the interference of acoustic waves, which create a speckle pattern as long as wave propagation occurs in the medium. A shadow represents a region where almost no acoustic interactions occur as the waves have been reflected at a preceding boundary and hence, speckle is minimum. The analysis of speckle in shadows can potentially provide a robust definition of the existence of a shadow, compared to previous literature which visually define a shadow as a bright boundary followed by a continuous dark region in B-mode (Kremkau and Taylor, 1986). The visual definition of a shadow can lead to inconsistent identification of exactly where a shadow begins, particularly by manual detection.

FUTURE STUDIES STUFF

### Conclusions

RF and B-mode methods were developed for acoustic shadow detection requiring only the transducer pulse width as the input parameter. When comparing to manual detection, the methods achieved a Dice similarity coefficient of 0.90±0.07 for RF detection and 0.87±0.08 for B-mode detection. indicating high similarity. The work

focused on applying shadow detection and statistical analysis to a varied dataset of three different anatomical locations and two different transducer to provide a representative understanding of general acoustic shadows. The versatility of the shadow detection method has potential to improve the interpretation of ultrasound images with shadow artifacts or to serve as a pre-processing step for machine learning methods in the future. However, the statistics indicate that the visual definition of shadows may not be robust as the bright boundary of a shadow, previously used to indicate the start of a shadow, has a non-negligible thickness and gradual brightness changes.

# References

Becker DM, Tafoya CA, Becker SL, Kruger GH, Tafoya MJ, Becker TK. The use of portable ultrasound devices in low- and middle-income countries: a systematic review of the literature. Tropical Medicine & International Health, 2016;21:294–311.

Bouhemad B, Brisson H, Le-Guen M, Arbelot C, Lu Q, Rouby JJ. Bedside ultrasound assessment of positive end-expiratory pressure-induced lung recruitment. American Journal of Respiratory and Critical Care Medicine, 2011;183:341–347.

Burckhardt CB. Speckle in ultrasound B-mode scans, 1978.

Byra M, Nowicki A, Wróblewska-Piotrzkowska H, Dobruch-Sobczak K. Classification of breast lesions using segmented quantitative ultrasound maps of homodyned K distribution parameters. Med. Phys., 2016;43:5561–5569.

Destrempes F, Cloutier G. A critical review and uniformized representation of statistical distributions modeling the ultrasound echo envelope. Ultrasound Med. Biol., 2010;36:1037–1051.

Galiano K, Obwegeser AA, Bodner G, Freund M, Maurer H, Kamelger FS, Schatzer R, Ploner F. Ultrasound guidance for facet joint injections in the lumbar spine: A computed tomography-controlled feasibility study. Anesthesia and Analgesia, 2005;101:579–583.

Ghose S, Oliver A, Mitra J, Martí R, Lladó X, Freixenet J, Sidibé D, Vilanova JC, Comet J, Meriaudeau F. A supervised learning framework of statistical shape and probability priors for automatic prostate segmentation in ultrasound images. Medical Image Analysis, 2013;17:587–600.

Good LI, Edell SL, Soloway RD, Trotman BW, Mulhern C, Arger Pa. Ultrasonic properties of gallstones. Effect of stone size and composition. Gastroenterology, 1979;77:258–263.

Hellier P, Coupé P, Morandi X, Collins DL. An automatic geometrical and statistical method to detect acoustic shadows in intraoperative ultrasound brain images. Medical Image Analysis, 2010;14:195–204.

Hetherington J, Lessoway V, Gunka V, Abolmaesumi P, Rohling R. SLIDE: automatic spine level identification system using a deep convolutional neural network. International Journal of Computer Assisted Radiology and Surgery, 2017;12:1189–1198.

Ho MC, Lin JJ, Shu YC, Chen CN, Chang KJ, Chang CC, Tsui PH. Using ultrasound Nakagami imaging to assess liver fibrosis in rats. Ultrasonics, 2012;52:215–222.

Karamalis A, Wein W, Klein T, Navab N. Ultrasound confidence maps using random walks. Medical Image Analysis, 2012;16:1101–1112.

Kremkau FW, Taylor KJ. Artifacts in ultrasound imaging. Journal of Ultrasound in Medicine, 1986;5:227–237.

Milletari F, Ahmadi SA, Kroll C, Plate A, Rozanski V, Maiostre J, Levin J, Dietrich O, Ertl-Wagner B, Bötzel K, Navab N. Hough-CNN: Deep learning for segmentation of deep brain regions in MRI and ultrasound. Computer Vision and Image Understanding, 2017;164:92–102.

Tuthill TA, Sperry RH, Parker KJ. Deviations from rayleigh statistics in ultrasonic speckle. Ultrasonic Imaging, 1988;10:81–89.

# Figure Captions

**Figure 1:** The Nakagami parameter maps computed and compared to the a) B-mode image and d) echo envelope. The echo envelope contains the unfiltered speckle that can be analyzed by statistical distributions.

**Figure 2:** A comparison of the detected shadows from the RF method, B-mode method, and manual detection. It is important to differentiate between a shadow and attenuation. In subfigure b), the RF method performs more accurately in identifying scanlines 32-64 as attenuation, rather than shadow. This is likely due to pixel intensity methods previously being dependent on multiple filtering kernels tuned for different anatomy and depth settings.
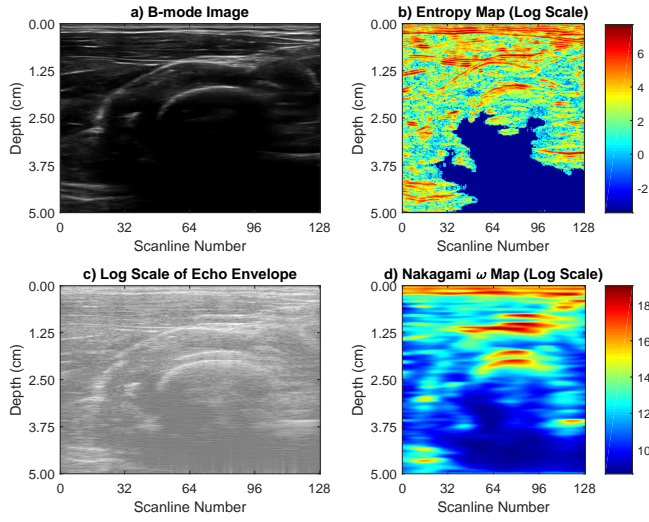
# Tables

**Table 1:** Transducer properties for different imaging scenarios.

|  | Anatomy | Frequency | Depth | Gain |
|---|---|---|---|---|
| **Linear Transducer (L14-5/38)** | Forearm | 11.0MHz | 5.0cm | 50% |
| | Elbow | 11.0MHz | 5.0cm | 40% |
| | Ribcage | 5.0MHz | 10.0cm | 30% |
| **Curvilinear Transducer (C5-2/60)** | Forearm | 4.0MHz | 5.0cm | 50% |
| | Elbow | 4.0MHz | 5.0cm | 40% |
| | Ribcage | 3.3MHz | 10.0cm | 30% |

**Table 2:** Mean Dice coefficients for different imaging scenarios $\pm$ standard deviation.

|  |  | **RF** | **B-Mode** |
|---|---|---|---|
| Linear (L14-5/38) | Forearm | 0.91±0.05 | 0.89±0.06 |
| | Elbow | 0.94±0.06 | 0.90±0.07 |
| | Ribcage | 0.87±0.09 | 0.84±0.06 |
| Curvilinear (C5-2/60) | Forearm | 0.89±0.05 | 0.86±0.08 |
| | Elbow | 0.93±0.04 | 0.90±0.09 |
| | Ribcage | 0.83±0.08 | 0.83±0.10 |
| **Mean** | **All Anatomy** | **0.90±0.07** | **0.87±0.08** |